

Self-healing in $B_{12}P_2$ through mediated defect recombination

S. P. Huber,^{1,2,*} E. Gullikson,³ C. D. Frye,⁴ J. H. Edgar,⁴ R. W. E. van de Kruijs,² F. Bijkerk,² and D. Prendergast¹

¹*Molecular Foundry, Lawrence Berkeley National Laboratory, Berkeley, California 94720, United States*

²*Industrial Focus Group XUV Optics, MESA + Research Institute for Nanotechnology, University of Twente, P.O. Box 217, 7500 AE, Enschede, The Netherlands*

³*Center for X-Ray Optics, Lawrence Berkeley National Laboratory, Berkeley, California 94720, United States*

⁴*Department of Chemical Engineering, Kansas State University, Manhattan, Kansas 66506, United States*

(Dated: Wednesday 9th November, 2016)

The icosahedral boride $B_{12}P_2$ has been reported to exhibit “self-healing” properties, after transmission electron microscopy recordings of sample surfaces, that were exposed to highly energetic particle beams, revealed little to no damage. In this work, employing calculations from first-principles within the density functional theory (DFT) framework, the structural characteristics of boron interstitial and vacancy defects in $B_{12}P_2$ are investigated. Using nudged elastic band simulations, the diffusion properties of interstitial and vacancy defects and their combination, in the form of Frenkel defect pairs, are studied. We find that boron icosahedra maintain their structural integrity even when in a degraded state in the presence of a vacancy or interstitial defect and that the diffusion activation energy for the recombination of an interstitial vacancy pair, can be as low as 3 meV, in line with the previously reported observation of “self-healing”.

I. INTRODUCTION

The semiconductor $B_{12}P_2$, also referred to as icosahedral boron phosphide, is part of a group of boron-rich solids that form a class of superhard materials^{1,2} that, at their core, largely share the crystalline structure of α -rhombohedral boron. The ground state structures of these borides are generally thought to be well understood, although more stable ground states are still being found, as in the recent case of B_6O_2 .³ The fundamental building block of these borides, is a structural unit of 12 boron atoms, whose crystallographic sites are defined by the 12 vertices of a convex regular icosahedron. The simplest crystalline boron allotrope, α -rhombohedral boron, is formed by an rhombohedral arrangement of these boron icosahedra. Icosahedral boron phosphide, is one of the many boron-rich solids that is a direct derivative of α -rhombohedral boron. In these solids, the icosahedral network is interspersed by dimers of phosphorus, arsenic or oxygen atoms, as in $B_{12}P_2$, $B_{12}As_2$ or $B_{12}O_2$ respectively, or trimers of a combination of boron and carbon atoms, as in B_4C and $B_{13}C_2$.

Due to their strongly related crystal structures, with the boron icosahedron at its foundation, these boron-rich materials share many interesting structural properties such as a high melting temperature and radiation hardness, making them ideal candidates for radiation resistant applications. In particular, the borides with pnictide inter-icosahedral dimers, $B_{12}P_2$ and $B_{12}As_2$, have been found to be extremely resistant to damage induced by high energy particle radiation⁴. Samples were irradiated by highly energetic electrons for several hours at room and lowered temperatures, however, post-irradiation transmission electron microscopy measurements of the sample surfaces revealed little to no signs of structural degradation. Under the conditions of the experiment, it was estimated that each boron atom, on average, was displaced at least several times for the

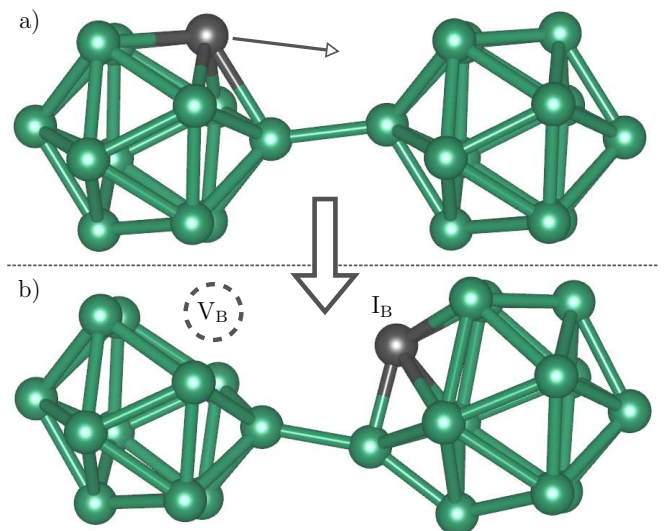


FIG. 1. (Color online) Schematic representation of boron Frenkel defect creation in an icosahedral boride. The top panel (a) represents two unperturbed boron icosahedra where the boron atom marked by a black sphere just received a large momentum in the direction of the arrow, transferred by a high energy particle in an inelastic scattering event. The bottom panel (b) shows the situation after the inelastic scattering event where a boron atom is displaced, forming an interstitial defect I_B while leaving a vacancy defect V_B behind.

duration of the exposure. A schematic depiction of a boron atom displacement as a result of a collision with a high energy particle is displayed in Fig. 1. Combined with the observed lack of structural damage, the conclusion was drawn that there must be a mechanism of “self-healing”, that restores damage caused by the displacement of boron atoms and is active even in low thermal energy systems.

The high radiation hardness, as a result of this “self-

healing” mechanism, makes these materials interesting for a variety of applications such as beta-voltaic devices⁵ and, combined with the relatively high neutron capturing cross-section of boron, neutron detectors^{6,7}. However, to the best of the authors’ knowledge, there has been no further experimental or theoretical research on the underlying mechanisms that give rise to this extraordinary “self-healing” property. The most obvious suggestion is that any boron vacancy and interstitial defect pair, commonly referred to as a Frenkel pair or Frenkel defect, created by a high energy collision, has both a high energy cost for creation and a low activation energy for recombination.

In this work, we will discuss the diffusion behavior of boron vacancy and interstitial defects, and combinations of the two to form Frenkel defect pairs, from first principles within the density functional theory (DFT) framework. Our results will show that boron icosahedra are highly resilient atomic building blocks and maintain structural integrity even when in a degraded state in the presence of either a boron vacancy or interstitial defect. Employing nudged elastic band (NEB) calculations, we have investigated potential intra-icosahedral diffusion paths of vacancy and interstitial defects and calculated the diffusion activation energies. Combining a vacancy and interstitial defect into a Frenkel defect, NEB simulations are employed to determine potential recombination pathways, which will reveal that activation energies for the recombination of the Frenkel defect, separated on different icosahedra, can be as low as 3 meV, potentially explaining the experimentally observed radiation hardness.

II. COMPUTATIONAL METHOD

A. Structural relaxation

All structural optimizations have been carried out within the DFT framework using the Vienna *ab initio* simulation package VASP⁸. Core electrons are replaced by ultrasoft pseudopotentials within the projector augmented wave (PAW) method^{9,10} where the $2s$ and $2p$ electrons for boron and the $3s$ and $3p$ electrons for phosphorus are treated as valence electrons. The generalized gradient approximation (GGA) as formulated by Perdew-Burke-Ernzerhof (PBE)¹¹ is employed for the exchange-correlation energy. A $2 \times 2 \times 2$ supercell from the $B_{12}P_2$ unitcell was used for all calculations, totalling 288 boron and 48 phosphorus atoms for the perfect crystalline supercell. Plane waves were expanded up to an energy of 400 eV and the Brillouin zone was sampled at the Γ point, unless stated otherwise. All structures, with and without structural defects, were optimized by minimizing the Hellmann-Feynman forces acting on the nuclei below the threshold value $0.02 \text{ eV } \text{\AA}^{-1}$.

B. Nudged elastic band

Nudged elastic band (NEB) calculations employed the climbing image method in combination with an improved tangent definition^{12,13}, implemented as an extension of the previously mentioned software package VASP. Initial and final images for any NEB calculation were relaxed until all atomic forces were below the threshold value of $0.02 \text{ eV } \text{\AA}^{-1}$. The initial guess for the NEB pathway was generated from the relaxed initial and final image, by linearly interpolating the atomic positions, where all resulting images are equidistant in terms of their relative Cartesian distance, unless explicitly stated otherwise. The relaxation threshold value, during the relaxation of all the images along the pathway under constraint of the imposed elastic band, was increased to $0.03 \text{ eV } \text{\AA}^{-1}$. During the relaxation process, the Brillouin zone was sampled at the Γ point, but to compute the total energies of the relaxed images, the k -point density was increased to a $2 \times 2 \times 1$ Monkhorst-Pack mesh¹⁴, in order to ensure convergence better than $2 \times 10^{-2} \text{ meV}$ per atom.

C. Molecular dynamics

All molecular dynamics have been carried out with VASP with identical values for the relevant DFT parameters described in section II A on the method of structural relaxation. For the simulation of the dynamics of Frenkel defect recombination, a $2 \times 2 \times 2$ $B_{12}P_2$ supercell including a single boron interstitial of type I_B^A , was first equilibrated at the target temperature by coupling the system to a Nosé-Hoover thermostat and sampling the canonical ensemble (NVT). The time step was set to 0.2 fs. After an equilibration period of 3 ps, the thermostat was decoupled and the microcanonical ensemble (NVE) was sampled for another 2 ps. From that point in time, in intervals of 1 ps, a vacancy was introduced at positions described in greater detail in the main text, and the system, that now includes a full Frenkel defect, was sampled for 1 ps.

D. Charged defects

Periodic boundary conditions provide an effective method of simulating pristine crystals within density functional theory. However, this approach has the downside that it introduces spurious interactions between local aperiodicities, such as structural defects, and their periodic images, unless the simulated cell is sufficiently large to render these interactions negligible. Additionally, structural defects in solid state materials can exist in various charge states and the long-ranged Coulomb interaction between the localized charge density and its periodic image can lead to significant inaccuracies in computed energies¹⁵. Correcting for these spurious interactions is

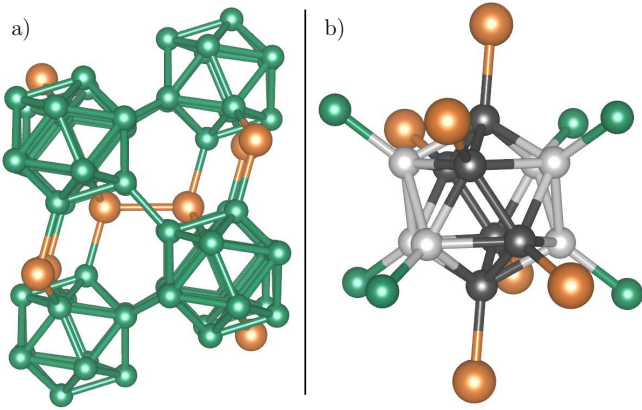


FIG. 2. (Color online) (a) A schematic depiction of the crystal structure of $B_{12}P_2$, where orange spheres represent phosphorus atoms and green spheres represent boron atoms. This depiction shows six complete boron icosahedra in a rhombohedral formation with one complete phosphorus dimer positioned in the center. Panel (b) depicts a single complete icosahedron with twelve external B and P atoms it is bound to. Boron atoms bound to an external boron atom (B-bound) are indicated by a light grey sphere, whereas boron atoms bound to an external phosphorus atom (P-bound) are indicated by black spheres. Boron-boron, boron-phosphorus and phosphorus-phosphorus bonds are drawn up to a maximum of 2, 2 and 3 Å, respectively.

non-trivial and several methods have been proposed^{16–20}, however no single rigorous correction method is currently available. This work will also consider charged defects but the calculated total energies will not explicitly be corrected for the fictitious charge induced terms. However, since only energy differences between systems with an identical charge state are used, the introduced error cancels out and the omission of an explicit correction is justified.

III. RESULTS

A. Crystal structure

A schematic representation of the crystal structure of $B_{12}P_2$ is shown Fig. 2. In this work, we consider the hexagonal unit cell, which contains 36 boron and 6 phosphorus atoms. The optimized lattice parameters a and c are 5.998 nm and 11.843 nm, respectively, which compare well to the experimental values of 5.987 nm and 11.847 nm reported in literature²¹. As mentioned in the introduction, the structure is formed by boron icosahedra that form an rhombohedral lattice with phosphorus dimers in between. The crystal structure has only three symmetrically unique crystal lattice sites, a phosphorus site, a boron site externally bound to a boron atom from another icosahedron and a boron site bound to a phosphorus atom. These different boron sites will be referred

to as P-bound and B-bound boron sites and are shown in Fig. 2 (b) as black and light gray spheres, respectively. Note that the B-bound boron sites are organized in two groups of three on opposing sides of the icosahedron and the P-bound boron atoms form a connected chain along the icosahedron, and these distinct groups of icosahedral atoms will be referred to as the poles and equator of the icosahedron, respectively. This asymmetry will prove to play an important role in the diffusion characteristics of interstitial defects, which will be discussed later in this work.

B. Interstitial and vacancy defects

To study the diffusion characteristics of interstitial and vacancy point defects, one first needs to determine their equilibrium positions within the crystalline host cell. The two unique boron lattice sites in the $B_{12}P_2$ crystal structure, give a total of 2 symmetrically unique boron vacancy defects, a B-bound boron vacancy $V_{B(B)}$ and a P-bound vacancy $V_{B(P)}$. In stark contrast with vacancy point defects, which occupy lattice sites of the crystal host by definition, the locations of interstitial point defects are not known *a priori*. A reasonable initial guess, are positions within the crystal unit cell that are farthest removed from all occupied lattice sites, as positions that are too close to other atoms are unlikely to be thermodynamically stable. To determine these positions for $B_{12}P_2$, an interstitial boron atom was placed randomly within the unit cell, which was subsequently moved by a simplex algorithm to maximize its first-nearest neighbor distance. This process was repeated many times and a histogram of the optimized first-nearest neighbor distances, for all the randomly sampled starting interstitial positions, is shown in Fig. 3 (a). The positions within the crystalline unit cell, corresponding to the four most abundant first-nearest neighbor distances, labeled $A - D$ in Fig. 3 (a), are shown in Fig. 3 (b) and 3 (c).

Interstitial positions $A - C$ all have six symmetrically equivalent positions in the unit cell and interstitial position D is located in the center of the icosahedron. A $2 \times 2 \times 2$ supercell was constructed with a single interstitial boron atom for each of the four different starting positions shown in Fig. 3, and the atomic positions were optimized by minimizing the Hellman-Feynman forces, acting on every individual atom, below $0.02 \text{ eV } \text{Å}^{-1}$. Parts of the relaxed structures, including the interstitial boron atom, are shown in Fig. 4.

The interstitials A and D relax to the same final structure, shown in Figs. 4 (a) and 4 (c), where the interstitial boron atom is fully incorporated in the icosahedron. The interstitial atom is located in the center of the triangle formed by the three B-bound boron atoms at the pole of the icosahedron, and is fully fivefold coordinated with icosahedral boron atoms, but does not form a bond with any extra-icosahedral atoms. To accommodate the interstitial, the B-bound atom indicated by the black sphere

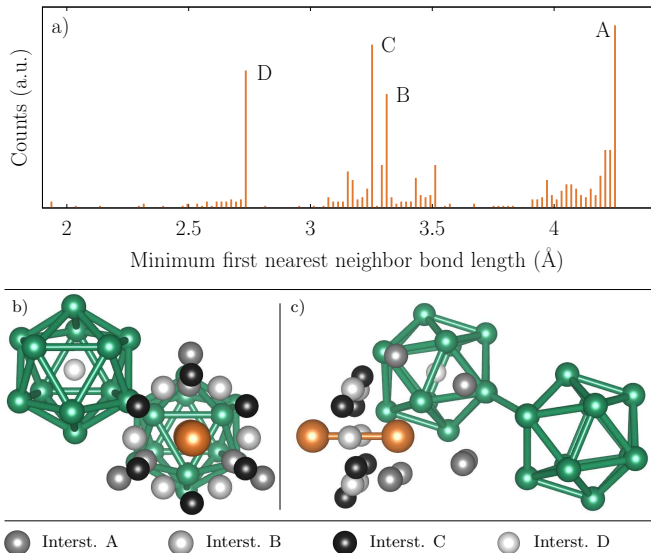


FIG. 3. (Color online) Histogram of optimized minimum nearest-neighbor distance of a boron interstitial for thousand randomly sampled starting positions. The most abundant optimized distances, labeled $A - D$, have the corresponding position within the unit cell shown (b) and (c). Site A has 6 symmetrically identical positions within the unit cell. Sites B and C both have 6 symmetrically equivalent positions forming a buckled hexagon with the phosphorus dimer oriented along its center axis. Site D is located at the center of the icosahedron.

in Figs. 4(a) and 4(c), is significantly displaced to the point where it is no longer fivefold but fourfold coordinated with icosahedral atoms.

Interstitial B and C also relax to an identical configuration, as shown in Figs. 4(b) and 4(d). The interstitial boron atom is located next to an icosahedron, to which it is twofold coordinated. The directly adjacent phosphorus dimer maintains its orientation along the $\langle 001 \rangle$ direction, but is significantly stretched to almost 3 \AA to allow both P atoms to coordinate with the interstitial. The interstitial and P dimer form an almost perfect isosceles triangle with the boron-phosphorus bonds, with length 1.87 \AA , as the legs and a vertex angle $\angle PBP$ of 104.8° .

The two interstitial boron configurations as described in this section will be referred to as interstitial A (I_B^A) and interstitial B (I_B^B), respectively, throughout the rest of this work, where the subscript indicates the elemental type of the defect and the superscript is a label. We have created each one of the two interstitial and vacancy defects, in a $2 \times 2 \times 2$ $B_{12}P_2$ supercell and the formation energies of the relaxed defects I_B^A and I_B^B , are 4.84 eV and 5.06 eV , respectively. The vacancy defects $V_{B(B)}$ and $V_{B(P)}$, have very similar formation energies at 5.02 eV and 5.45 eV , respectively. All of the defect structures relaxed with only minor deformations of the defective icosahedron or any of the directly neighboring icosahedra, which shows that a boron icosahedron maintains structural integrity even when in a degraded state in the presence of vacancy

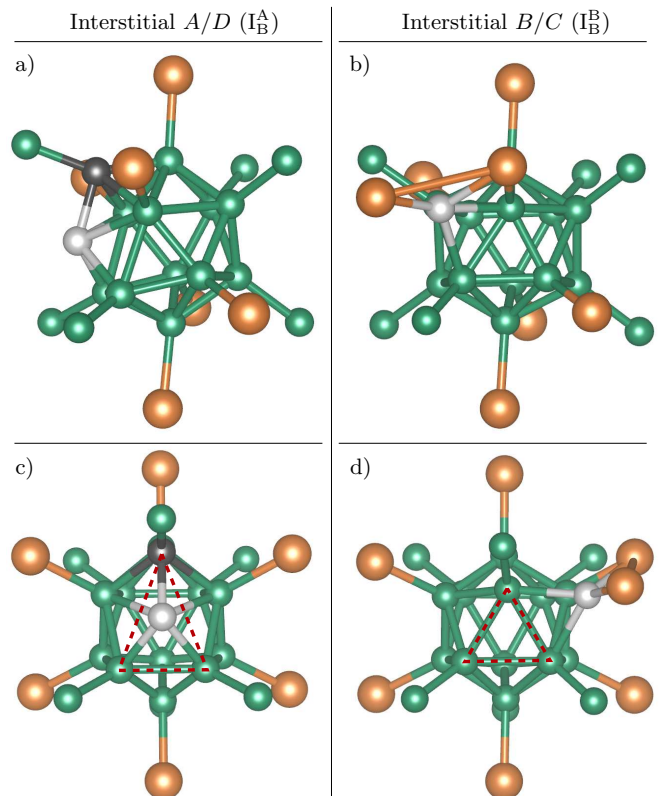


FIG. 4. (Color online) Side (a,b) and front (c,d) views of part of the relaxed supercells containing an interstitial boron atom. Interstitials A/D and B/C relax to the structures shown in (a,c) and (b,d), respectively, where the labels $A - D$ refer to the starting position of the interstitial atom before relaxation and correspond to the labels in Fig. 3. The light gray sphere indicates the interstitial atom and the black sphere in (a) and (c) indicates the undercoordinated B-bound atom.

or interstitial defect.

C. Frenkel defect recombination pathways

Now that we have obtained the equilibrium positions of vacancy and interstitial defects within the $B_{12}P_2$ unit cell, we can start to investigate potential recombination pathways of a vacancy and interstitial defect pair, often referred to as a Frenkel defect or Frenkel pair. In this work, we assume the existence of such a Frenkel defect and do not presuppose anything about the event that created the defect and as such our starting situation is a perfect $B_{12}P_2$ crystal with a single boron vacancy defect and a single boron interstitial, that are not necessarily located on the same icosahedron. Due to computational resource and time constraints, we limit the investigation to Frenkel defects with an interstitial defect of type I_B^A . The formation energies indicate that this interstitial is thermodynamically more stable compared to I_B^B , and therefore one can make the assumption that Frenkel recombination involving I_B^A interstitials, will

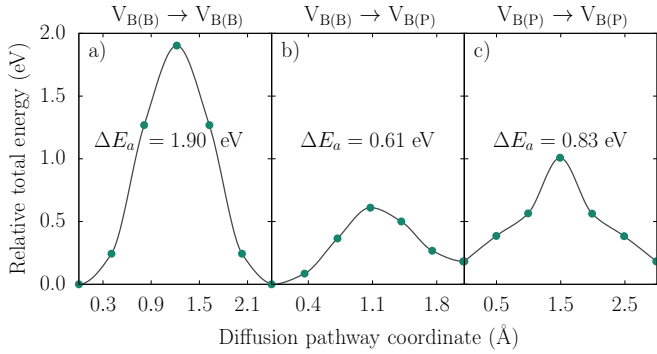


FIG. 5. (Color online) Diffusion pathways of a boron vacancy to a neighboring position on the same icosahedron from a (a) boron- to boron-bound site, (b) boron- to phosphorus-bound site and (c) a phosphorus- to phosphorus-bound site. The green points represent the total energy of the image along the diffusion pathway relative to the initial image and the solid line, computed by a piecewise cubic hermite interpolating polynomial, serves as a guide to the eye. The reaction coordinate of each image represents its total Cartesian distance relative to the initial image.

serve as an upper limit for diffusion barrier energies of Frenkel defect recombination in general. Even when limiting the discussion to Frenkel defects consisting of an I_B^A interstitial and one of the two distinct boron vacancies, computing all combinations and potential recombination pathways would be computationally prohibitive. Instead, the full recombination process can be split into three subprocesses: (1) the diffusion of the vacancy, (2) the diffusion of the interstitial and finally (3) the diffusion of the interstitial to the vacancy and the recombination of the Frenkel pair.

D. Vacancy diffusion

In the process of vacancy diffusion, we can distinguish between inter-icosahedral and intra-icosahedral vacancy diffusion, which correspond to migration of the vacancy site between two different icosahedra or within an icosahedron, respectively. For intra-icosahedral diffusion of a boron vacancy to a directly neighboring lattice site, there are three distinct possibilities: $V_{B(B)}$ to $V_{B(B)}$, $V_{B(B)}$ to $V_{B(P)}$ and $V_{B(P)}$ to $V_{B(P)}$, where the notation $V_{B(P)}$ indicates a vacancy at a P-bound boron site. The diffusion pathways for each one of these three vacancy diffusion combinations have been computed using a nudged elastic band calculation, with 5 intermediate images along the pathway between the initial and final image, and the energy barrier profiles are shown in Fig. 5.

The diffusion activation energy ΔE_a is defined as

$$\Delta E_a = E_m - E_i, \quad (1)$$

where E_i is the total energy of the initial image and E_m is the maximum energy along the diffusion pathway. Intra-icosahedral boron vacancy diffusion has the

Defect	d_{ico} (Å)	d_{ext} (Å)	d_{tot} (Å)	$l(B-B)$ (Å)
$V_{B(B)} \rightarrow V_{B(B)}$	0.63	0.56	1.20	1.67 1.68
$V_{B(B)} \rightarrow V_{B(P)}$	0.35	0.62	0.97	1.79 1.73
$V_{B(P)} \rightarrow V_{B(P)}$	0.52	0.54	1.06	1.73 1.73

TABLE I. Structural parameters for the image along the diffusion pathway where the total relative energy is at a maximum for the three different types of vacancy diffusion. The second and third column show the summed distance in Å traveled by atoms, with respect to their position at the start of the diffusion pathway, from the defective icosahedron (excluding the diffusing atom itself) and from atoms that are a direct neighbor to the defective icosahedron, respectively, and the fourth column is the sum of these two distances. The final column shows the boron bond lengths in Å of the diffusing atom.

lowest activation energy when the initial and final vacancy site are boron sites bound to opposite elements, as can be seen in Fig. 5 (b), where diffusion of a boron- to phosphorus-bound vacancy has a diffusion barrier of 0.61 eV, and 0.43 eV in the opposite direction. The diffusion barrier for the $V_{B(P)}$ to $V_{B(P)}$ pathway is, at 0.83 eV, only slightly larger, but contrastingly, the $V_{B(B)}$ to $V_{B(B)}$ diffusion barrier is significantly larger at 1.90 eV. This strong asymmetry in diffusion activation energies is somewhat surprising, as at a first glance the defect structures along the different pathways look similar. Upon closer inspection, differences can be found however and certain structural parameters that capture the asymmetry are displayed in Table I.

The columns labeled d_{ico} and d_{ext} represent the displacement of atoms in the image with the highest energy with respect to the initial image (i.e. the image in the middle of the diffusion pathway), for atoms of the icosahedron containing the vacancy and its directly neighboring external atoms, respectively. This value for the icosahedral atoms, is a direct measure of the distortion of the icosahedron under the influence of the diffusing vacancy and is a factor of two larger for the $V_{B(B)} \rightarrow V_{B(B)}$ pathway compared to the $V_{B(B)} \rightarrow V_{B(P)}$ pathway. The reason for the increased icosahedral distortion can be traced back to the strongly contracted boron bond lengths of the diffusing boron atom (compared to the equilibrium boron-boron bond length of 1.79 Å in the perfect crystal) as displayed in the last column of Table I. In the image with the highest energy along the pathway, the diffusing boron atom has exactly two neighboring boron atoms with which it forms a bond and therefore each row in the last column of Table I contains two values, corresponding to the lengths of those boron bonds. The increased icosahedral distortion, due to contracted boron bond lengths of the diffusing boron atom, explains the

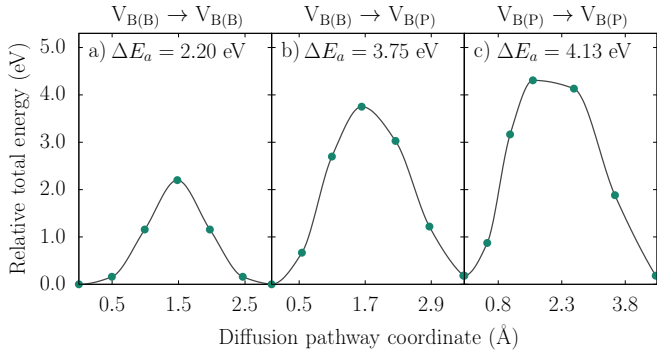


FIG. 6. (Color online) Diffusion pathways of a vacancy to a position on a neighboring icosahedron from a (a) boron- to boron-bound site, (b) boron- to phosphorus-bound site and (c) a phosphorus- to phosphorus-bound site. The green points represent the total energy of the image along the diffusion pathway relative to the initial image and the solid line, computed by a piecewise cubic hermite interpolating polynomial, serves as a guide to the eye. The reaction coordinate of each image represents its total Cartesian distance relative to the initial image.

significant energy barrier difference between the three different vacancy diffusion paths.

With a diffusion barrier of almost 2 eV, the $V_{B(B)} \rightarrow V_{B(B)}$ diffusion pathway is unlikely to occur, however the $V_{B(B)} \rightarrow V_{B(P)}$ pathway has an energy barrier that is certainly surmountable. Combined with the fact that a vacancy at any vertex on the icosahedron can reach all other vertices, solely by $V_{B(B)} \rightarrow V_{B(P)}$ diffusion, we find that a vacancy can diffuse intra-icosahedrally at a cost of approximately 0.55 eV per step.

For inter-icosahedral vacancy diffusion, we consider the same three variations as discussed for inter-icosahedral diffusion in the previous section, and we will limit the discussion to lattice position pairs with the shortest possible distance. The results are shown in Fig. 6. The activation barriers for all considered inter-icosahedral vacancy diffusion pathways are significantly larger, compared to their corresponding intra-icosahedral analogs. At multiple eV at least, these diffusion events are highly unlikely to occur spontaneously or due to thermally activated processes. Even for the shortest diffusion pathway $V_{B(B)} \rightarrow V_{B(B)}$, which models the diffusion of a polar boron atom to the closest polar position on its directly neighboring icosahedron, an activation barrier of 2.2 eV ensures that the probability of this diffusion process occurring is negligible.

E. Interstitial diffusion

In this section, we will discuss interstitial diffusion, which we will limit to intra-icosahedral interstitial diffusion, since we have seen from inter-icosahedral vacancy diffusion, that the migration of boron atoms between icosahedra is costly and unlikely to occur. In section III B, we described the interstitial boron positions in the

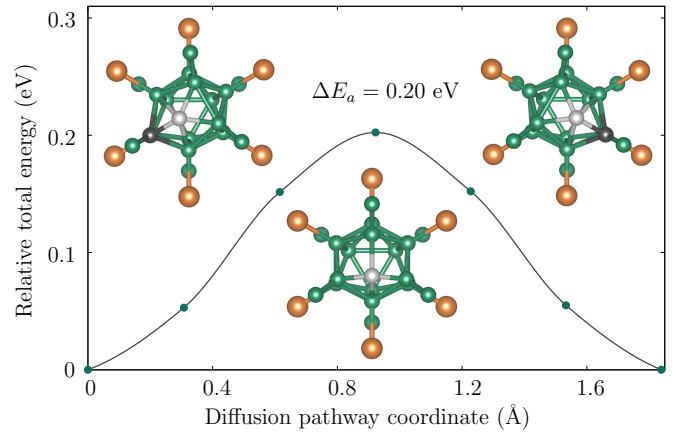


FIG. 7. (Color online) Diffusion barrier for polar interstitial diffusion with the total energy of each image, relative to the initial image, plotted as a function of the coordinate of the image along the diffusion pathway. The solid line serves as a guide to the eye. The structural configurations from left to right correspond to the initial, middle and final image along the diffusion pathway, respectively.

$B_{12}P_2$ unit cell. When discussing the diffusion of interstitial defects, in the context of a Frenkel defect and its recombination, we only consider the most thermodynamically stable interstitial I_B^A . In this interstitial configuration, one could consider the interstitial atom to be either the added atom without any extra-icosahedral bonds, or the displaced atom with a fourfold intra-icosahedral undercoordination, shown as light and dark gray spheres in Fig. 4 (a) and (c), respectively. A more useful interpretation is to consider both these atoms as an interstitial pair and to study their combined intra-icosahedral diffusion behavior. We recall the pattern found in the elemental types of directly neighboring atoms of the boron icosahedron [see Fig. 2 (b)], where the B-bound atoms are grouped into two triangles at the poles of the icosahedron and the P-bound boron atoms form a connected ring along the equator. The interstitial pair is formed by one of the atoms of the polar triangle and an atom in the center of the triangle, and symmetry dictates that there are six symmetrically equivalent configurations of this interstitial pair.

Interstitial diffusion can then be defined as the process where the interstitial pair transitions between any of these six configurations, which again due to symmetry can be reduced to two distinct diffusion pathways: (1) diffusion within the same polar triangle (polar diffusion) or (2) diffusion from one pole, across the icosahedral equator to the opposing pole (cross-equatorial diffusion). The diffusion pathway for polar interstitial diffusion as calculated with the NEB method, is shown in Fig. 7. The structural configurations of the initial, middle and final image along the diffusion pathway show that the relative ordering of the atoms is maintained and the distortion of the polar triangle, due to the presence of the interstitial atom, is merely transferred to the other vertex of the tri-

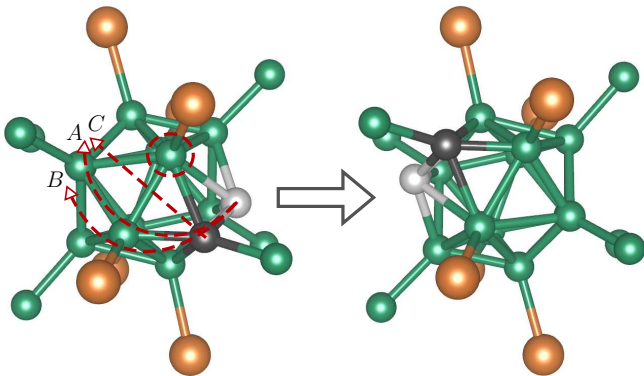


FIG. 8. (Color online) From left to right, the initial and final image for cross-equatorial interstitial diffusion. The atoms belonging to the interstitial pair are represented by light and dark gray spheres as in all previous figures. The red arrows labeled, A , B and C represent a schematic pathway along which the atoms diffuse. For pathways A and B both atoms of the interstitial pair move along the direction of the arrow, pushing neighboring boron atoms along the direction of the arrow, across the icosahedron equator. The arrow labeled C indicates a diffusion pathway where only the interstitial atom, marked by the dark gray sphere, diffuses directly across the equator.

angle by a skewing motion. As such, the required atomic displacement for the diffusion of the interstitial pair is minimal and the diffusion activation energy, at 0.20 eV , is relatively low compared to vacancy diffusion. Through this skewing motion, the interstitial pair can thus reach any of the two other configurations on the same pole, and with that, reach half the space bordering the icosahedron, at a minimal energy cost.

In the case of cross-equatorial interstitial diffusion, the interstitial pair has to diffuse from one pole of the icosahedron to the other, crossing the icosahedron's equator. The initial and final image of such an interstitial diffusion pathway are shown in Fig. 8.

A migration of the interstitial atom directly through the center of the icosahedron will have too large an energy barrier and will be a highly unlikely event. Alternatively, the interstitial pair can migrate over the surface of the icosahedron, effectively by moving over to the directly adjacent occupied icosahedral vertex, pushing its current occupant towards the other side of the equator. Two of such pathways, labeled A and B , have been schematically indicated by red arrows in Fig. 8, where the diffusing atoms will move roughly along the direction of the arrow. It is important to note that the atoms of the interstitial pair in the initial image, indicated by the light and dark gray spheres, do not actually move to the other pole themselves but rather they move along the direction of the arrow, pivoting around the P-bound atom highlighted by a red circle, pushing atoms along their way across the equator. Contrastingly, the arrow labeled C , represents a diffusion pathway where the dark gray atom directly crosses the equator. The diffusion barriers for

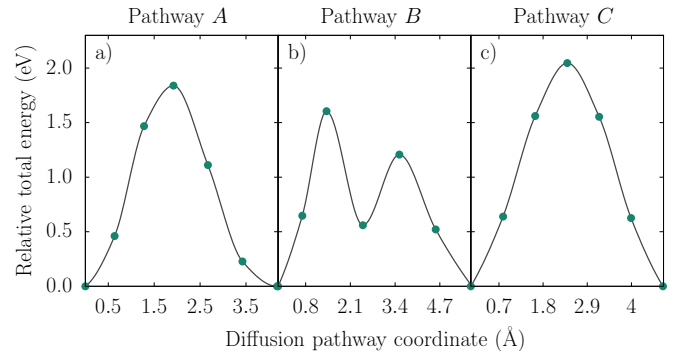


FIG. 9. (Color online) Equatorial interstitial diffusion barriers for pathways (a) A , (b) B and (c) C from Fig. 8. The green points indicate the total energy of the image relative to the initial image as a function of the pathway coordinate of the image. The solid curve serves as a guide to the eye.

the three different pathways A , B and C are shown in Fig. 9 (a-c), respectively.

Compared to the polar interstitial diffusion, the energy barriers for cross-equatorial interstitial diffusion are significantly higher at 1.6 eV to 2.1 eV . This is understandable as for cross-equatorial diffusion the total atomic displacement along the pathway is significantly larger and during diffusion bonds are broken. The structure of the system that causes the local minimum in the middle of the diffusion path of pathway B [see Fig. 9 (b)], corresponds directly to the configuration of interstitial I_B^B , as shown in Fig. 4. These three diffusion pathways have the smallest diffusion energy barrier possible for cross-equatorial interstitial diffusion and therefore it is likely that, once an interstitial of type I_A^A is formed on a certain pole of an icosahedron, it is most likely trapped on that side of the equator.

In summary, we find that cross-equatorial diffusion of an interstitial pair is unlikely due to a high diffusion activation energy, which is in stark contrast with polar diffusion which, with a diffusion barrier of a mere 0.20 eV is more likely to occur. Despite the icosahedral equator formed by P-bound boron atoms acting like a barrier for interstitial diffusion, preventing an interstitial pair from easily diffusing to the opposing pole, it can still reach half of the space directly adjacent to the icosahedron through polar interstitial diffusion.

F. Frenkel defect recombination

With the analysis of the diffusion behavior of vacancy and interstitial defects completed, we can now turn to the final part of Frenkel defect diffusion; the recombination of the interstitial with the vacancy. The most likely diffusion paths of the interstitial atom will be those where the vacancy lies on the face of an icosahedron directly facing the pole of the interstitial pair. For any other paths, the interstitial will have to diffuse around or through icsa-

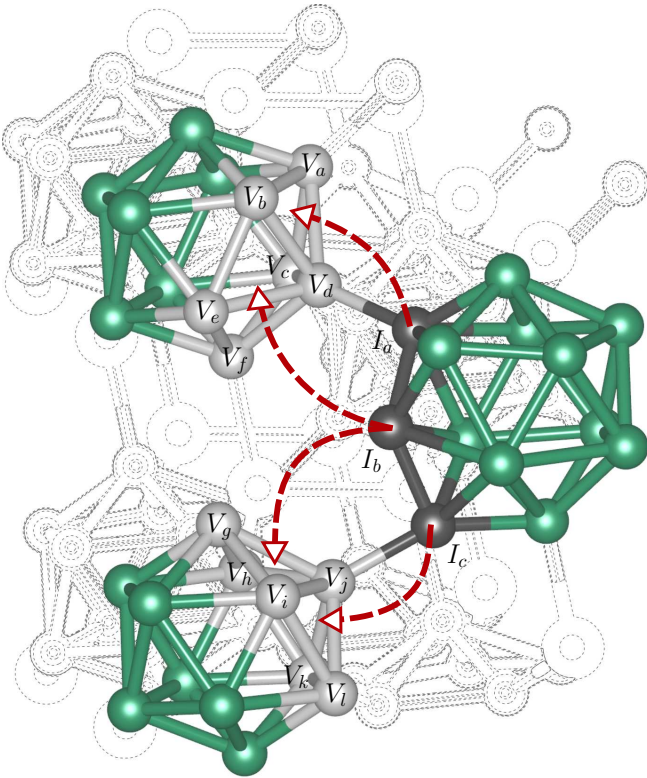


FIG. 10. (Color online) Atomic positions considered for the interstitial and vacancy defects of Frenkel pairs, indicated by dark gray and light gray spheres and labeled $I_a - I_c$ and $V_a - V_l$, respectively. The red arrows indicate the pairing up of the interstitials I_a , I_b and I_c with vacancies from the groups $V_a - V_f$, $V_a - V_l$ and $V_g - V_l$, respectively.

hedra or phosphorus dimers, and would therefore be energetically costly and unlikely to occur.

We consider an interstitial defect of type I_B^A , which has three directly neighboring icosahedra, two of which have a symmetrically identical orientation with respect to the boron interstitial pair. There are three boron atoms on the interstitial pole that have a symmetrically unique orientation with respect to neighboring icosahedra, indicated by dark gray spheres in Fig. 10, and labeled I_a , I_b and I_c . Potential vacancy defect sites are sites on the icosahedral faces that are directly adjacent to the interstitial defect, marked by light gray spheres in Fig. 10 and labeled V_a through V_l . The labels V_a through V_l and I_a through I_c merely serve as indices to identify their corresponding crystal lattice sites. Recombination pathways are considered for Frenkel defects where the interstitials I_a , I_b and I_c are paired up with a vacancy from the groups $V_a - V_f$, $V_a - V_l$ and $V_g - V_l$, respectively, as indicated by the arrows in Fig. 10, giving a total of 24 Frenkel pairs.

For every Frenkel pair combination, the initial and final image of its corresponding recombination pathway, are the cell containing a Frenkel defect and the perfect crystal, respectively. The initial recombination pathway was constructed with six linearly interpolated images be-

tween the fully relaxed initial and final image, giving a total of 8 images labeled 0 through 7, where 0 corresponds to the initial image. A requirement of the NEB method, is that both the initial and final image, from which the intermediate pathway is constructed, are fully relaxed. In this case, relaxing the final image is trivial, since that always constitutes the perfect crystal where the Frenkel defect has fully recombined. Contrastingly, there is no guarantee that the initial image containing the Frenkel defect has a (meta)-stable state, which as it turns out is the case for 4 out of the 24 Frenkel defect configurations that we considered. For Frenkel defects with a vacancy at either V_d or V_j , no stable state exists and the defect always spontaneously recombined and therefore a meaningful recombination pathway could not be computed and the activation barrier for the recombination of these Frenkel defects is effectively zero. This is not wholly surprising, considering that the boron atoms at vacancy positions V_d and V_j are the interconnecting atoms to the interstitial containing icosahedron, and are the closest to that icosahedron out of all the considered vacancy positions.

Interestingly, all other Frenkel defects do have a (meta)-stable state and the initial image could be fully relaxed without spontaneous recombination, and an attempt to find a relaxed diffusion pathway through a NEB calculation could be made. This shows that boron icosahedra are remarkably robust and remain stable, maintaining their structural integrity, even in the presence of a boron vacancy or interstitial defect and that due to the stability of these Frenkel defects, the diffusion pathway now has an activation energy that needs to be overcome, for recombination to occur. With the exception of four Frenkel defect pairs, $I_b \rightarrow V_a$, $I_b \rightarrow V_b$, $I_b \rightarrow V_k$ and $I_b \rightarrow V_l$, a relaxed diffusion recombination pathway could be found, from which an activation energy barrier could be extracted, as shown in Table II. The reason that no relaxed solution could be found for the four aforementioned Frenkel recombination pathways is directly related to the fact that the corresponding vacancy positions are the furthest removed from the interstitial atom [see Fig. 10]. Moreover, the direct diffusion pathway from the interstitial to these vacancy positions is blocked by the boron-boron bond that interconnects the two involved icosahedra, which act as a barrier to the interstitial atom.

When constructing an initial guess for the recombination pathway of a Frenkel pair, the most straightforward assumption is that the interstitial atom diffuses directly to the position of the vacancy. However, this pathway is not necessarily the only possible pathway nor the most energetically favorable. This is best illustrated by an example, so we consider the recombination of Frenkel pair $I_c \rightarrow V_g$. The initial guess of the directly diffusing pathway will have interstitial I_c diffuse directly to the vacancy at position V_g . However, one could also imagine a pathway where the boron atom at V_j will diffuse to the vacancy at V_g , after which interstitial I_c will diffuse

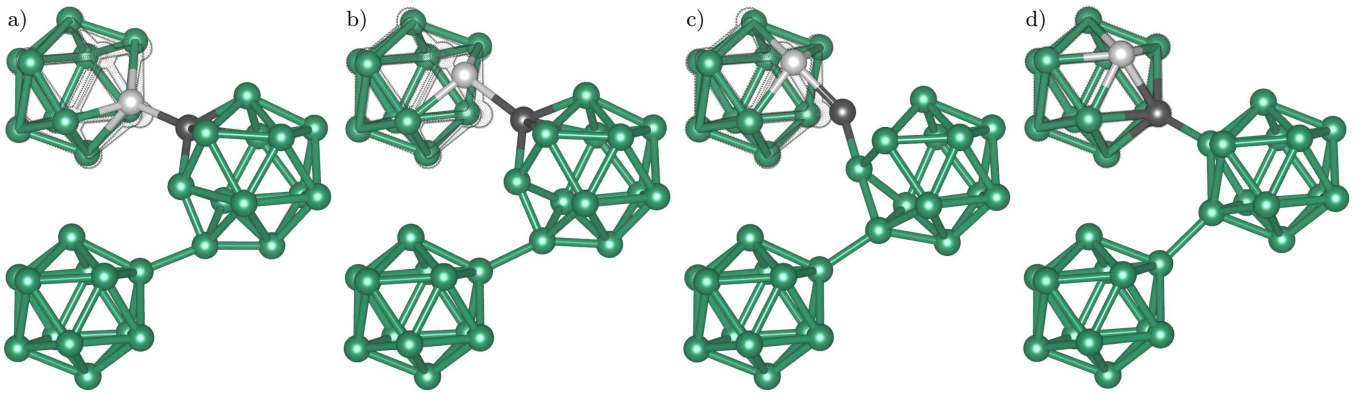


FIG. 11. (Color online) (a–d) Partial structures of the initial, second, fourth and final image, respectively of the relaxed recombination pathway for the $I_a \rightarrow V_b$ Frenkel defect. The interstitial atom I_a is colored black and the mediating atom at position V_d is colored in light gray. All four images show a black mesh outline over the top left vacancy containing icosahedron, which traces the atoms of the icosahedron in its relaxed configuration in the final image. This serves as a guide to the eye, to indicate the relaxed atomic positions that the diffusing atoms will end up in.

Pair	ΔE_a	Mediated	Pair	ΔE_a	Mediated
$I_a \rightarrow V_a$	0.04	Yes	$I_b \rightarrow V_a$	–	–
$I_a \rightarrow V_b$	0.003	Yes	$I_b \rightarrow V_b$	–	–
$I_a \rightarrow V_c$	0.24	Yes	$I_b \rightarrow V_c$	0.25	Yes
$I_a \rightarrow V_d$	×	×	$I_b \rightarrow V_d$	×	×
$I_a \rightarrow V_e$	0.31	Yes	$I_b \rightarrow V_e$	0.31	Yes
$I_a \rightarrow V_f$	0.38	Yes	$I_b \rightarrow V_f$	0.40	No
$I_c \rightarrow V_g$	0.39	Yes	$I_b \rightarrow V_g$	0.02	No
$I_c \rightarrow V_h$	0.16	Yes	$I_b \rightarrow V_h$	0.31	No
$I_c \rightarrow V_i$	0.16	Yes	$I_b \rightarrow V_i$	0.31	No
$I_c \rightarrow V_j$	×	×	$I_b \rightarrow V_j$	×	×
$I_c \rightarrow V_k$	0.23	No	$I_b \rightarrow V_k$	–	–
$I_c \rightarrow V_l$	0.23	No	$I_b \rightarrow V_l$	–	–

TABLE II. Diffusion activation energies ΔE_a of recombination pathways of various Frenkel pairs in eV. The interstitial and vacancy labels of the Frenkel pairs directly correspond to the labels in Fig. 10. Frenkel pairs without a stable state and therefore without a meaningful activation energy for their recombination are marked by \times . Frenkel pairs with a (meta)-stable state but for which no relaxed recombination pathway was found through the NEB algorithm are indicated by a dash.

to the newly created vacancy at V_j . The final images of these two scenarios are completely indistinguishable, however their recombination pathways, with activation energies of 1.41 eV and 0.39 eV, respectively, are distinctively unique. These two types of pathways, where either the interstitial atom diffuses directly, or the recombinatorial diffusion is mediated by one or more other boron atoms, will be referred to as “direct” and “mediated” diffusive recombination, respectively.

The column labeled “Mediated” in Table II indicates whether the given activation energy corresponds to a mediated or direct diffusion recombination pathway. For some Frenkel pairs, both a direct and a mediated pathway could be found, in which case the one with the lowest activation energy is listed. In general, when pathways of both types were found, the mediated pathway had a lower activation energy, with the noticeable exception of $I_c \rightarrow V_k$ and $I_c \rightarrow V_l$, for which the mediated activation energy is significantly larger at 0.68 eV, compared to the 0.23 eV of the direct recombination pathway.

A schematic representation of a mediated recombination pathway is shown in Fig. 11, which depicts four images of the $I_a \rightarrow V_b$ recombination pathway. The leftmost panel in Fig. 11, represents the initial image which contains a Frenkel defect, with the vacancy at position V_b and the interstitial atom I_a , whereas the rightmost panel shows the final image where the Frenkel defect is recombined and the structure is a perfect crystal once again. The structures in Figs. 11 (b) and 11 (c) represent images along the pathway between the initial and final image. Interstitial atom I_a is shown in black and the boron atom at position V_d is indicated as a light gray sphere, which highlights that the diffusion of interstitial I_a to the vacancy containing icosahedron, is in fact mediated by the diffusion of the atom at V_d to the vacancy at V_b . Effectively then, this Frenkel recombination process is a summation of two separate diffusive processes, an intra-icosahedral vacancy- and an inter-icosahedral interstitial diffusion, that operate synchronously. The seamless coordination of these two diffusive processes in the case of $I_a \rightarrow V_b$, culminates in a negligible activation energy barrier of a mere 3 meV for the recombination of the Frenkel defect.

The energy profile of a recombination pathway can be defined as the total energy of every image along the relaxed recombination pathway, relative to the initial image, as a function of the total cartesian distance of the

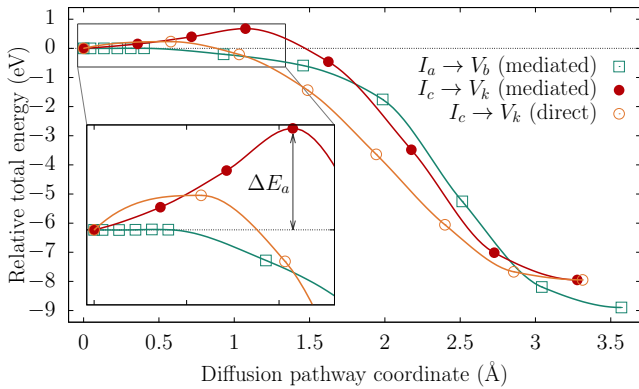


FIG. 12. (Color online) Energy profiles for three Frenkel recombination pathways. The symbols represent the total energies of the images along the pathway in eV, relative to the initial image, as a function of the image’s total Cartesian distance in Å, with respect to the initial image. The solid line serves as a guide to the eye and the inset shows a close up of the region where the total energy of the pathways reaches a maximum.

image with respect to the initial image. Three examples, including the energy profile for the $I_a \rightarrow V_b$ recombination pathway that has just been discussed, are shown in Fig. 12.

The activation energy, indicated by ΔE_a in Fig. 12, is clearly visible for both the $I_c \rightarrow V_k$ pathways, but is almost indiscernible for $I_a \rightarrow V_b$. As mentioned previously, for the majority of Frenkel defects, the mediated recombination pathway often had a smaller activation energy compared to the direct recombination pathway. The pathways for $I_c \rightarrow V_k$ (and identically for $I_c \rightarrow V_l$ which is not shown) are the exception, where the activation energy is significantly larger for the mediated recombination pathway. In general, all the relaxed recombination pathways for the Frenkel pairs considered, have an energy profile with a similar shape. An initial monotonic incline in energy, which represents the activation energy barrier for the recombination, followed by a steep monotonic decline in energy, reaching a minimum for the final image. However, for the Frenkel defects $I_a \rightarrow V_b$ and $I_b \rightarrow V_g$, the entire energy profile of the recombination pathway was descending. Therefore a value for the activation energy could not be extracted, even though it is certain that the pathway has a non-negligible barrier, given that the defect was initially stable. For these Frenkel defects, the relaxed recombination pathway was used as a starting point for a second iteration, where additional images were added between the first and second image and the NEB method was used to relax this new pathway. The inset in Fig. 12 shows the additional images for the $I_a \rightarrow V_b$ Frenkel defect, from which the actual recombination activation energy of 3 meV was determined.

The total energy of the final image is equal for all recombination pathways, as it is the total energy of the perfect crystal. The fact that the relative energies for

the final images of the pathways, plotted in Fig. 12, are not equal, is due to the fact that these are relative to the total energy of the initial image of their respective Frenkel defect, which varies slightly between the different Frenkel pair configurations, but is typically approximately 8.9 eV higher compared to the perfect crystal. This energy difference corresponds directly to the formation energy of the Frenkel pair and this is also the energy that will be released into the system upon the recombination of the Frenkel defect. The effect on the crystal structure of the sudden release of such an amount of energy, will certainly not be negligible and will be interesting for further study, however the simulation of these dynamics are beyond the scope of this work. The study of the dynamics of a system with a Frenkel defect prior to its recombination, however, is possible and of interest. Moreover, entropic effects due to the vibrational modes of the system are not properly described in the NEB method, however, these are explicitly accounted for in a molecular dynamics approach, provided that the system is sampled over sufficiently long time scales. The molecular dynamics approach therefore, though computationally expensive, provides a robust and valuable method of verifying the predicted free energy landscape by means of the NEB method.

G. Frenkel recombination dynamics

For the 24 Frenkel defect configurations discussed in the previous section, the nudged elastic band method determined that 4 Frenkel defects do not have a stable initial state, for 4 Frenkel defects no relaxed combination pathway could be found and for the remaining 16 defects, a recombination activation energy between 0.003 eV and 0.4 eV was found. A drawback of the NEB method is that the final relaxed pathway, if one can be found, is dependent on the initial guess for the pathway. In this work, the initial guess was a simple linear interpolation between the initial and final image, with optional atomic index swapping, but other than that the pathway was restricted to that initial guess within certain margins, through the constraints of the NEB method. Consequently, if the initial guess is too far off from what would be the true optimal recombination pathway, the wrong pathway may be found or no path may be found at all where one does exist. To verify the conclusions made from the NEB analysis, we studied the molecular dynamics of Frenkel defects prior to their recombination, which does not suffer from the bias introduced by the initial guess of the recombination process, which is inherent in the NEB method.

The starting configuration for all Frenkel defect recombination dynamics simulations, is a $B_{12}P_2$ supercell with a single I_B^A defect, equilibrated at the target temperature T as explained in detail in Section II C. After equilibration, whose point in time is set to be the origin $t = 0$, in intervals of 1 ps, for each of the 12 potential locations labeled $V_a - V_l$ in Fig. 10, a single vacancy was created

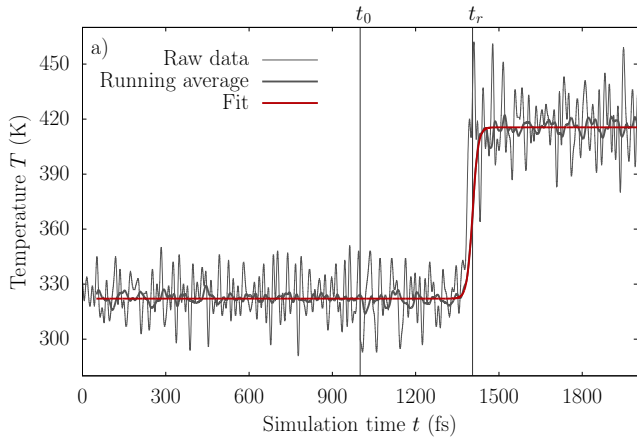


FIG. 13. (Color online) Evolution of the temperature during the micro-canonical ensemble sampling of a $B_{12}P_2$ system that initially includes a single interstitial boron atom. The dashed black line represents the raw temperature as taken from the molecular dynamics trajectory, whereas the solid black line represents a moving average of the former, with a window width of 250 steps, which corresponds to 50 fs. The solid red line is a fit of the function defined in Eq. 2 to the running average temperature. The first 1000 fs represent the final stage of the equilibration stage with just the interstitial defect, after which at t_0 , marked by a vertical dashed line, a boron vacancy is introduced. The system that now contains a full Frenkel defect is sampled further and after 1400 fs the temperature sharply increases as a direct result of the recombination of the Frenkel defect. The inflection point of the temperature increase, labeled t_r and marked by a vertical dashed line, is defined as the time of recombination of the Frenkel defect.

and the micro-canonical ensemble was sampled for a further 1 ps. The time of the creation of the vacancy with respect to $t = 0$ is denoted as t_0 .

If, during the 1 ps of sampling after the introduction of the vacancy defect, the Frenkel defect recombines, a release of approximately 8.9 eV of energy accompanying the recombination event, will be converted into kinetic energy, by virtue of conservation of energy imposed by the micro-canonical ensemble. This increase in kinetic energy will raise the temperature of the system significantly. An example of the evolution of the temperature of the system as a function of time, for one of the simulated Frenkel defects, is shown in Fig. 13. The temperature of the interstitial containing system fluctuates around an average of approximately 325 K, during the equilibration period. At t_0 the vacancy is introduced, creating a Frenkel defect. Approximately 400 fs later, the temperature increases rapidly as a direct result of the recombination of the Frenkel defect. The inflection point of the temperature increase, i.e. the point where the recombination process is at its halfway point is labeled t_r . We then define the defect lifetime of the Frenkel defect to be $\tau = t_r - t_0$. To extract this value from the temperature evolution, we define the temperature of the system

		V_a	V_b	V_c	V_d	V_e	V_f	V_g	V_h	V_i	V_j	V_k	V_l
t_0	T	Defect lifetime τ (fs)											
1	12	-	202	-	114	-	-	373	-	-	52	-	-
2	12	-	214	-	114	-	-	377	-	-	53	-	-
3	12	-	212	-	115	-	-	370	-	-	52	-	-
4	12	-	304	-	117	-	-	386	-	-	52	-	-
5	12	-	254	-	113	-	-	391	-	-	52	-	-
1	300	-	162	-	104	-	-	405	-	-	58	-	-
2	300	-	162	-	134	-	-	335	-	-	56	-	-
3	300	-	927	-	125	-	-	487	-	-	57	-	-
4	300	-	186	-	110	-	-	195	-	-	65	-	-
5	300	-	159	-	130	-	-	152	-	-	57	-	-
1	600	-	178	-	177	134	199	103	205	236	94	-	-
2	600	-	-	-	121	-	183	-	214	-	143	-	-
3	600	-	-	-	146	-	179	-	336	-	145	-	-
4	600	-	-	-	205	-	380	-	277	-	147	-	-
5	600	-	-	-	127	-	413	-	373	-	129	-	-

TABLE III. The time τ in fs between the creation of the vacancy defect t_0 and the recombination of the Frenkel defect for the twelve potential vacancy positions $V_a - V_l$, where the micro-canonical ensemble of the system is sampled at a temperature T in K. The vacancy creation time t_0 in ps is referenced with respect to $t = 0$ which marks the end of the equilibration of the system containing just the interstitial boron defect.

as a function of time as

$$T(t) = T_0 + Ae^{(t-t_r)/\sigma}. \quad (2)$$

Since there are high frequency temperature fluctuations in the raw data, we first take a moving average with a window size of 250 step, or 50 fs and fit Eq. 2 to the resulting data, using a least-squares optimization algorithm. The computed defect lifetimes for all the simulated Frenkel defects, defined by their vacancy position V_x , time of creation t_0 and temperature T , are listed in Table III, where a dash indicates that the defect did not recombine throughout the duration of the simulation.

Literature reports high energy particle exposure experiments not just for various boride and energetic particle combinations, such as lithium ion bombarded B_4C^{22} and electron exposed $B_{12}P_2^4$, but also for different experimental operating temperatures of 12 K²³, 91 K and 300 K⁴. All these experiments report a similar lack of defect agglomerations and structural damaging, even at lower temperatures, suggesting only a small amount of thermal energy is required to activate the recombination mechanism. Therefore we have performed the Frenkel defect recombination dynamics both at 12 K and 300 K.

At temperatures of 12 K and 300 K, just 4 out of 12

Frenkel defects recombine within the 1 ps of the simulation. The recombination pathways corresponded to $I_a \rightarrow V_b$, $I_a \rightarrow V_d$, $I_b \rightarrow V_g$ and $I_c \rightarrow V_j$ and did not change their character between runs. The Frenkel defects with a vacancy at either V_j or V_d , consistently recombine within the first 120 fs, which confirms the results from the NEB simulations that found that these particular Frenkel defects are not stable and recombine spontaneously. Frenkel defects with their vacancy defect at position V_b and V_g remained stable considerably longer, but both still recombined well within 1 ps of their creation. This observation confirms the NEB results discussed in the previous section, which predicted a negligible energy barrier for exactly these and only these Frenkel defect recombination pathways.

The NEB method also determined many Frenkel defect recombination pathways with a non-negligible activation energy, all of which did not recombine during the 1 ps of micro-canonical sampling. This is partly due to the fact that the thermal energy $k_B T$ at a temperature of 325 K is approximately 28 meV, which is lower than a significant subset of predicted activation energies tabulated in Table II. However, it can also be ascribed to the short simulation time of 1 ps which statistically may prevent the recombination event from being sampled. To illustrate this, we have repeated the same Frenkel defect recombination dynamics at an elevated temperature of 600 K. For the first run, all but 4 out of 12 defects recombine within the first few hundredths of femtoseconds of the simulation, showing that at elevated temperature more defects may recombine in a comparable time frame. However, we only found an increase in the number of Frenkel defects that recombined within the 1 ps of the simulation, for one of the runs at 600 K, which highlights that it is not just the available thermal energy but also the sampling duration that determines whether the recombination event will be sampled.

A remarkable difference in defect lifetimes, between the first run and the subsequent four runs at 600 K, is that for the latter, the Frenkel defects with a vacancy at position V_b and V_g and a finite lifetime at lower temperatures, no longer recombined. Similarly, defects with the vacancy at V_f and V_h , which never recombined at 12 K and 300 K, all of a sudden had a finite lifetime smaller than 1 ps. The explanation for this observation is not that the elevated temperature enable a new recombination mechanism, but rather, during the equilibration period at 600 K, the system underwent polar diffusion of the interstitial complex. We described this process in Section III E, where the icosahedral pole containing the interstitial boron atom, changes its orientation with respect to its neighboring icosahedra. The activation energy of this skewing motion is relatively low at 0.2 eV [see Fig. 7] and a closer inspection of the equilibration trajectory of the system at 600 K revealed that the polar interstitial diffusion occurred roughly every picosecond. At the moment that the vacancies were introduced for the first run at 600 K, the system was just transitioning

from the original interstitial orientation, on which the labeling in Fig. 10 is based, to another orientation. The apparent change in which defects recombine is therefore merely a result of the changed orientation of the interstitial pole that transforms the original labeling, which can be undone by a symmetrical transformation. The recombination pathways for runs 2 to 5 at 600 K with a vacancy at the positions V_f and V_h , correspond to the mediated $I_a \rightarrow V_b$ pathway visualized in Fig. 11. Similarly, defects labeled V_d and V_j had a recombination pathway that can be mapped to $I_a \rightarrow V_d$ on the original labeling. The fact that the system was in a structural transition at the moment of the first run at 600 K, also explains why more Frenkel defects recombined, since the structure was temporarily even further removed from its equilibrium position, opening access to other recombination channels.

Generally, the findings of the simulated dynamics of the Frenkel defects agree with the predicted activation energies for their recombination, presented in Section III F. Defects with a negligible activation energy all recombined within 1 ps of the molecular dynamics simulation and the other defects all remained in tact, in agreement with their predicted non-negligible activation energy and the relatively short simulation time of 1 ps. However, there is one particular defect that stands out. The NEB method predicted an activation energy of only 40 meV for the $I_a \rightarrow V_a$ recombination pathway, yet in none of the molecular dynamics simulations did this defect recombine. This defect then provides the perfect example to reiterate that it is not just the activation energy that determines whether a predicted recombination pathway will be sampled, but rather the specific motion required by that pathway may be unlikely to be sampled. Like the recombination of $I_a \rightarrow V_b$, as illustrated in Fig. 11, the recombination pathway for $I_a \rightarrow V_a$ is a mediated recombination. However, unlike in the case of $I_a \rightarrow V_b$, where the diffusive motion is limited to just two atoms that move in a similar direction for the entire pathway, the NEB determined recombination pathway for $I_a \rightarrow V_b$ hinges on the collaborative movement of at least three atoms, whose motion changes direction multiple times. This coordinated movement of multiple atoms in the predicted recombination pathway $I_a \rightarrow V_a$ is visualized in Fig. 14.

For this recombination to occur, first atom B_b has to move a significant distance towards B_a and B_c to form a threefold coordinated boron complex. Then a vacancy diffusion is required where B_a diffuses to the position V_a , while B_b and B_c remain mostly stationary. The recombination is completed finally by a motion of B_c that is directly perpendicular to the vacancy diffusion of B_a . The rather complicated nature of this sequence of events, characterized by motions that are mostly perpendicularly directed and nonsimultaneous, explains why the pathway that is defined by it, is not necessarily sampled, despite having a low activation energy.

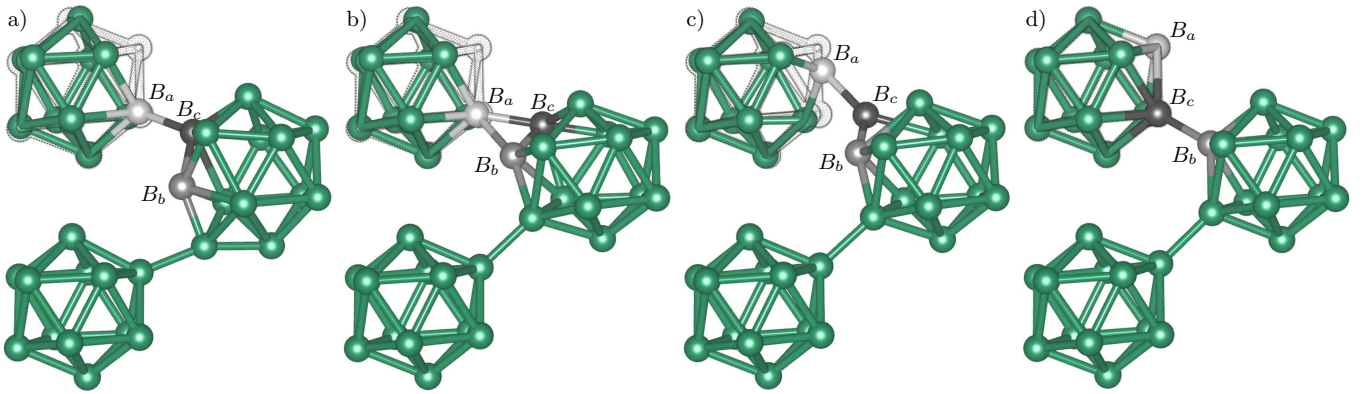


FIG. 14. (Color online) (a–d) Partial structures of the initial, third, fifth and final image, respectively of the relaxed recombination pathway for the $I_a \rightarrow V_a$ Frenkel defect. The boron atoms that are the main participants in the diffusive recombination are labeled B_a , B_b and B_c , and are represented by grey spheres, going from light to dark, respectively. All four images show a black mesh outline over the top left vacancy containing icosahedron, which traces the atoms of the icosahedron in its relaxed configuration in the final image. This serves as a guide to the eye, to indicate the relaxed atomic positions that the diffusing atoms will end up in.

H. Frenkel defect charge localization

To determine the charge density localization associated with the presence of a Frenkel defect, we have performed Bader analysis on the 10 stable Frenkel defects, which will yield an effective charge for each atom in the cell²⁴. For the bulk pristine crystal structure, the average number of valence electrons attributable to boron and phosphorus atoms is 2.92 and 5.43, respectively. This shows that on average the boron atoms lose a small amount of their original valence charge of 3 to the phosphorus atoms. When an interstitial boron defect is introduced, the overall valence numbers remain largely the same, however, the interstitial atom in the middle of the polar triangle (the atom labeled I_b in Fig. 10), with a Bader charge of 3.71, gains almost a full electron. At this point we introduce a vacancy at one of the 10 positions that will yield a complete and stable Frenkel defect. Interestingly, if the structure is not relaxed after introducing the vacancy, the change in Bader charges is almost negligible and the valence charge of the interstitial atom increases only slightly to 3.74 on average. However, if after introducing the vacancy, the atomic positions are relaxed, a significant change in Bader charges is observed. The computed effective valencies for the atoms on the vacancy containing icosahedron and the atoms on the interstitial containing icosahedral pole, are tabulated in Table IV.

Bader analysis shows that the boron atoms on the vacancy containing icosahedron will have a net charge of approximately +0.1, resulting in an overall +1 charge for the corresponding icosahedron. The electrons given up by the vacancy containing icosahedron are mostly transferred to the boron atoms of and directly adjacent to the interstitial defect, I_b and I_c . Just as these two atoms form a pair that define the interstitial defect from a geometric perspective, as explained in Section III E, so do they form a pair from a charge density perspective. The

Vacancy	Q_{vac}	Q_a	Q_b	Q_c	Q_d	Q_{int}
V_a	2.86	2.80	3.66	3.17	2.80	3.11
V_b	2.88	2.69	4.02	2.90	2.89	3.12
V_c	2.87	2.83	4.01	2.88	2.81	3.13
V_e	2.89	2.80	3.34	3.63	2.79	3.14
V_f	2.89	2.82	3.88	3.08	2.79	3.14
V_g	2.90	2.94	2.84	3.97	2.95	3.17
V_h	2.91	2.87	3.35	3.41	2.91	3.14
V_i	2.91	2.91	3.34	3.41	2.88	3.13
V_k	2.86	2.91	2.99	3.71	2.87	3.12
V_l	2.86	2.86	3.00	3.74	2.91	3.13

TABLE IV. Effective number of valence electrons for various boron atoms in a supercell containing a stable relaxed Frenkel defect, as obtained from Bader analysis. The column labeled Q_{vac} gives the average valency of all boron atoms on the vacancy containing icosahedron. The columns labeled Q_a through Q_d represents the valency of the boron atoms on the interstitial containing icosahedron, labeled I_a through I_d in Fig. 15, respectively. The final column Q_{int} corresponds to the average of the four columns directly preceding it.

creation of a Frenkel defect is paired with a significant charge transfer that will reside on the $I_b - I_c$ boron atom pair. When the vacancy resides on the bottom left icosahedron in Fig. 10, atom I_c has the largest net electronic charge varying from -0.97 to -0.40 . Conversely, for a Frenkel defect with its vacancy on the upper left icosahedron in Fig. 10, it is the atom labeled I_b that garners the largest charge ranging from -1.02 to -0.34 . In general, for any Frenkel defect, there is a large charge transfer from the vacancy containing icosahedron to the interstitial containing icosahedral pole, where the former and

I. Charged Frenkel defects

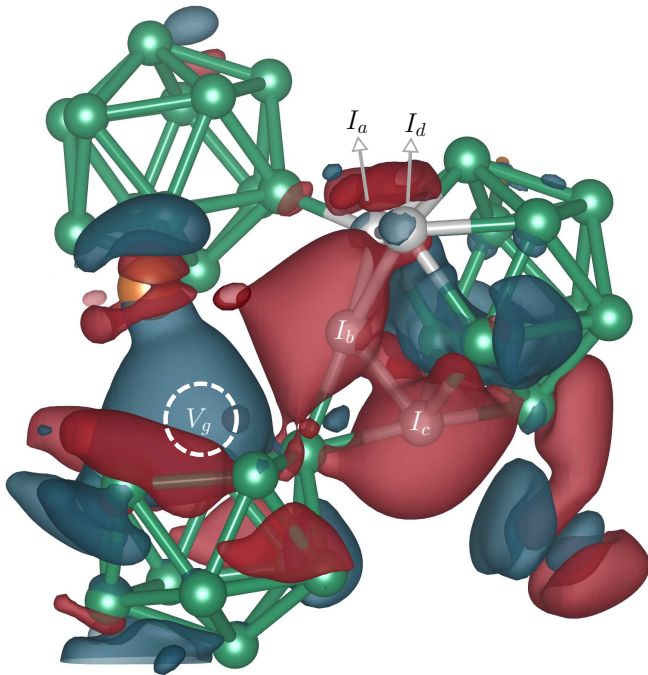


FIG. 15. (Color online) Isosurface visualization of the electron density difference between the $B_{12}P_2$ supercell containing a Frenkel defect with a vacancy at position V_g and the perfect crystal. The red and blue colors of the isosurfaces indicate where the electron density of the defective cell is larger and smaller compared to the bulk, respectively. In other words, locations in red (blue) show regions of the defective cell that have a net larger (smaller) electronic density compared to the bulk and therefore have a net negative (positive) charge. The specific Frenkel defect pictured has a vacancy at position V_g , indicated by the dashed white circle. The boron atoms on the icosahedron containing the interstitial defect are labeled I_a through I_d , whose corresponding effective valence charges as derived from Bader analysis, are displayed in Table IV under the columns labeled Q_a through Q_d , respectively

latter icosahedron effectively carry a total charge of +1 and -1 . To visualize this charge transfer, we have computed the charge density difference between the supercell containing a Frenkel defect and the perfect crystal. An isosurface representation of the charge density difference for the V_g Frenkel defect is shown in Fig. 15. Note that the isosurface shown is a representation of a charge density difference and not a pure charge density transfer, as it includes charge density differences that are simply induced by the displacement of atoms in creating the relaxed Frenkel defect. However, it does visually summarize the observed charge transfer from the vacancy containing icosahedron to the interstitial boron defect pair for all studied Frenkel defects.

The previous section highlighted that a Frenkel defect is accompanied by an intrinsic charge transfer from the vacancy containing icosadron to the interstitial containing icosahedron, but the overall charge of the system was maintained to be neutral, as it has been for all calculations discussed up till now. In reality however, structural defects, especially in semiconductors like $B_{12}P_2$, can exist in various charge states, which could potentially change the described defect recombination behaviour. Repeating all the calculations presented so far, for all possible charge states of the defect, would be an enormous and inefficient undertaking and moreover beyond the scope of this work. However, we can not leave the discussion about the potential influence of charged defects on the presented defect recombination mechanism untouched.

As a compromise, we have repeated the dynamics simulations, as presented for the neutral system in Section III G, for various charge states of the system at a temperature of 300 K. Defects created in semiconductors due to electron irradiation, as in the case of the experiment whose observation of self-healing we are trying to model⁴, are usually left in a positive charge state due to an overall depletion of electrons²⁵. Therefore, we consider the 12 possible Frenkel defects as described in Section III G, where the entire cell has an effective charge of +1, +2 or +3. We reduced the number of runs for each unique configuration from 5 to 3. The computed recombination times from the molecular dynamics trajectories are shown in Table V, which also include the corresponding results of the neutral cell of Table III at the same temperature for comparison.

The recombination times of three of the four defects which consistently recombined within 1 ps in a charge neutral system, i.e. V_d , V_g and V_j , remained comparable when a net positive charge was introduced to the system, indicating that the overall charge of the cell had little influence on the recombination dynamics. Contrastingly, the defect with a vacancy at V_b , which consistently recombined for a neutral system, remained stable for some of the runs of the positively charged cell. Interestingly, the exact opposite behavior was observed for defect V_a , which shares similarities with V_b in terms of the orientation of the interstitial defect with respect to the vacancy. Additionally, several defects, V_h , V_i , V_k and V_l , which were rarely observed to recombine for $Q = 0$, now all regularly recombined for $Q > 0$. In the way we verified the predicted recombination pathways through NEB calculations by explicitly running molecular dynamics in the first part of this work, we now reverse that process and further investigate the newly observed recombination dynamics of certain Frenkel defects by explicitly mapping the recombination pathway with the NEB method.

Since the vacancy pairs V_h-V_i and V_k-V_l are symmetrically equivalent, we have limited computing the recombination pathway for Frenkel defects in a charged cell with a vacancy at V_a , V_i or V_k . The molecular dynamics

t_0	Q	V_a	V_b	V_c	V_d	V_e	V_f	V_g	V_h	V_i	V_j	V_k	V_l
		Defect lifetime τ (fs)											
1	0	-	162	-	104	-	-	405	-	-	58	-	-
2	0	-	162	-	134	-	-	335	-	-	56	-	-
3	0	-	927	-	125	-	-	487	-	-	57	-	-
1	+1	-	258	-	106	-	-	127	-	-	57	562	222
2	+1	-	684	-	142	-	-	357	-	391	56	-	-
3	+1	-	-	-	133	-	-	150	-	-	58	362	-
1	+2	364	-	-	128	-	-	121	-	230	59	98	95
2	+2	325	779	-	224	-	-	392	-	485	59	113	110
3	+2	301	-	-	178	-	-	136	-	509	62	131	121
1	+3	306	-	-	189	-	-	147	506	938	62	100	97
2	+3	786	-	-	858	-	-	494	987	-	62	114	111
3	+3	333	-	-	179	-	-	457	606	-	64	135	124

TABLE V. The time τ in fs between the creation of the vacancy defect t_0 and the recombination of the Frenkel defect for the twelve potential vacancy positions $V_a - V_l$, where the micro-canonical ensemble of the system is sampled at a temperature of 300 K and the overall cell has an effective charge Q . The vacancy creation time t_0 in ps is referenced with respect to $t = 0$ which marks the end of the equilibration of the system containing just the interstitial boron defect.

trajectories showed that all recombination events were mediated recombinations of I_a or I_c , except for V_i where the direct recombination through I_b was also observed. Therefore we have computed the recombination pathways $I_b \rightarrow V_i$, $I_c \rightarrow V_i$, $I_a \rightarrow V_a$ and $I_c \rightarrow V_k$ for systems with a net charge Q of +1 to +3. The obtained activation energies for the recombination pathways are shown in Table VI.

For all recombination pathways, the activation energy, almost unilaterally, decreases as the net charge of the system becomes more positive. This decrease in activation energy for these particular recombination pathways, explains why the defects recombined in the molecular dynamics simulations of the positively charged cells, but remained stable in the neutral case. In summary, the charge state of Frenkel defects does clearly affect the recombination dynamics, however, the nature of the recombination mechanism, the mediated diffusion of vacancy and interstitial boron defects, remains unchanged compared to neutral defects. The charge state of the defect merely changes the local free energy landscape which determines which recombination pathways are energetically accessible.

To understand why the positive charge states for the defect recombination pathways listed in Table VI, result in such a significant reduction of the activation barrier compared to the neutral defects, we have computed the

Pair	ΔE_a			
	$Q = 0$	$Q = +1$	$Q = +2$	$Q = +3$
$I_b \rightarrow V_i$	0.31	0.11	0.07	0.06
$I_c \rightarrow V_i$	0.16	0.15	0.02	0.00*
$I_a \rightarrow V_a$	0.04	0.05	0.00*	0.009
$I_c \rightarrow V_k$	0.68	0.03	-	-

TABLE VI. Diffusion activation energies ΔE_a of recombination pathways of various Frenkel pairs in eV. The interstitial and vacancy labels of the Frenkel pairs directly correspond to the labels in Fig. 10. The activation energies equal to zero (marked by an asterisk) correspond to recombination pathways that were monotonically decreasing in energy for the original number of images. Since a meta-stable initial image was found for these Frenkel configurations, the energy maximum had to be located between the first two images, however, even after adding up to 8 images in between these first two images, a well-defined energy maximum still could not be found. This implies that the true activation energy for these recombination pathways is on the order of 1 meV.

Bader charges for the initial images of those pathways. By comparing the charge densities of the neutral cell with the positively charged cells, we find that the reduced overall charge affects the effective charge of the atoms throughout the entire cell and is not necessarily concentrated at the atoms near the Frenkel defect. Additionally, the atomic Bader charge difference is comparable in magnitude for both boron and phosphorus atoms and the average absolute atomic charge difference is on the order of 0.03 ± 0.03 for all Frenkel defects listed in Table VI. Despite the overall charge state of the cell affecting the majority of atoms in the cell, the largest absolute charge density differences are in fact localized on the two defective icosahedra, particularly on the interstitial containing icosahedron and yet again the interstitial boron defect pair I_b - I_c play the most prominent role. For all Frenkel defects, the interstitial defect pair is subjected to the largest absolute charge difference (within the pair itself) on the order of approximately 0.5, roughly one order of magnitude larger compared to the average value.

For the $I_b \rightarrow V_i$ and $I_c \rightarrow V_i$ recombination pathways, we observe a significant charge transfer from atom I_b to atom I_c . As Fig. 15 showed for the V_g Frenkel defect in its neutral charge state, as a result of the creation of the defect, a significant and comparable charge density is located on atoms I_b and I_c , resulting in the comparable effective number of valence electrons of 3.34 and 3.41, respectively (see Table IV). As the overall charge of the cell becomes more positive, valence charge is transferred from I_b to I_c , as much as 0.5 for the +3 charged cell, yielding an effective valence charge difference between I_b and I_c as big as 1 e. Despite these large local charge transfers, as a result of the overall charging of the cell, the average effective valence charges of the boron atoms of

the two defective icosahedra Q_{vac} and Q_{int} (see Table IV), remain almost completely unchanged. A similar effect is observed for $I_a \rightarrow V_a$, where an increasingly positive cell is accompanied by an increased charge transfer from I_b to I_c , as well as to the boron atom that would have been bound to the atom at the position of the vacancy. The defect corresponding to $I_c \rightarrow V_k$ exhibits a charge transfer in the opposite direction, where I_b becomes more electronegative at the expense of I_c .

$B_{12}P_2$ systems with a Frenkel defect exhibit multiple defect states within the electronic band gap, which would be those most likely to be emptied upon positively charging the system. However, the subsequent atomic rearrangement which minimizes the energy of the system prevents us from associating the nature of those defect states with the resulting charge configuration of the defect. Ultimately, it appears that the preferred charge state of the Frenkel defect as a whole is conserved, even when the overall system charge is being reduced slightly. From this simple analysis, it is impossible to extract the sole and definitive cause behind the lowering of the activation energy for the recombination of these particular defects. However, it does show that introducing an effective charge to the cell, leads to a significant and highly localized charge transfer between the two boron atoms that make up the interstitial defect, which likely plays the most significant role in the changes in the free energy landscape, which result in lowered activation energies for certain Frenkel defect recombination pathways.

IV. CONCLUSIONS

In this work, we have investigated the static structural properties of boron vacancy and interstitial point defects in the icosahedral boride $B_{12}P_2$ and found that degraded icosahedra that contain either a vacancy or an interstitial defect, remain stable and maintain their icosahedral structure. Using nudged elastic band calculations, the mobility of vacancy and interstitial defects was studied, which revealed that the majority of intra-icosahedral diffusion pathways of both defect types have a high activation energy barrier and are unlikely to occur, with the notable exception of the polar diffusion of an interstitial boron defect of type I_B^A .

Following the study of vacancy and interstitial mobility individually, the mobility of a combination of these two point defects in the form of a Frenkel defect pair,

was investigated. We have shown that all Frenkel configurations have a (meta-)stable state, except when the vacancy is located on the boron site that is directly bound to icosahedral face containing the interstitial boron atom, in which case the Frenkel defect will spontaneously recombine. For all other considered Frenkel pairs, various possible recombination pathways were modeled with the nudged elastic band method, which showed that certain Frenkel defects had an activation energy for recombination as low as 3 meV. The surprisingly low energy barrier is the cumulative result of two diffusion processes operating synchronously, where the inter-icosahedral diffusion of the interstitial boron is mediated by the intra-icosahedral vacancy diffusion of another boron atom. The Frenkel defect recombination pathways determined with the NEB method, have been verified by explicitly running molecular dynamics for the various defect configurations. The extracted lifetimes from these trajectories agreed to a high degree with the predicted activation energies.

We have also shown that the particular charge state of the defect does affect the recombination behavior, however, it does not alter the fundamental mediating character underlying the recombination mechanism. The charge state of the defect merely influences the local free energy landscape that makes certain recombination pathways energetically more easily accessible, while making others energetically more costly, increasing the Frenkel defect's effective lifetime. The demonstration of the mediated recombination mechanism for Frenkel defects, with activation energies of the order of just a few meV, corroborate earlier experimental results on the "self-healing" properties of $B_{12}P_2$.

ACKNOWLEDGMENTS

This work is supported by NanoNextNL, a micro and nanotechnology programme of the Dutch Government and 130 partners. We acknowledge the support of the Center for X-ray Optics of Lawrence Berkeley Laboratory and the Industrial Focus Group XUV Optics at the MESA+ Institute for Nanotechnology at the University of Twente, notably the partners ASML, Carl Zeiss SMT GmbH, and the Foundation FOM. All the computational work was performed at the Molecular Foundry which is supported by the Office of Science, Office of Basic Energy Sciences, of the United States Department of Energy under Contract No. DE-AC02-05CH11231.

* mail@sphuber.net

¹ Q. An and W. A. Goddard, *Chem. Mater.* **27**, 2855 (2015).

² Q. An, K. M. Reddy, H. Dong, M.-W. Chen, A. R. Oganov, and W. A. Goddard, *Nano Lett.* **16**, 4236 (2016).

³ H. Dong, A. R. Oganov, Q. Wang, S.-N. Wang, Z. Wang, J. Zhang, M. M. D. Esfahani, X.-F. Zhou, F. Wu, and

Q. Zhu, *Scientific Reports* **6**, 31288 (2016).

⁴ M. Carrard, D. Emin, and L. Zuppiroli, *Phys. Rev. B* **51**, 11270 (1995).

⁵ D. Emin, *J. Solid State Chem.* **179**, 2791 (2006).

⁶ J. C. Lund, F. Olschner, F. Ahmed, and K. S. Shah, *MRS Online Proc. Libr.* **162**, 601 (1989).

- ⁷ T. P. Viles, B. A. Brunett, H. Yoon, J. C. Lund, H. Hermon, D. Buchenauer, K. McCarty, M. Clift, D. Dibble, and R. B. James, *MRS Online Proc. Libr.* **487**, 585 (1997).
- ⁸ G. Kresse and J. Furthmüller, *Phys. Rev. B* **54**, 11169 (1996).
- ⁹ P. E. Blöchl, *Phys. Rev. B* **50**, 17953 (1994).
- ¹⁰ G. Kresse and D. Joubert, *Phys. Rev. B* **59**, 1758 (1999).
- ¹¹ J. P. Perdew, K. Burke, and M. Ernzerhof, *Phys. Rev. Lett.* **77**, 3865 (1996).
- ¹² G. Henkelman, B. P. Uberuaga, and H. Jónsson, *J. Chem. Phys.* **113**, 9901 (2000).
- ¹³ G. Henkelman and H. Jónsson, *J. Chem. Phys.* **113**, 9978 (2000).
- ¹⁴ H. J. Monkhorst and J. D. Pack, *Phys. Rev. B* **13**, 5188 (1976).
- ¹⁵ H.-P. Komsa, T. T. Rantala, and A. Pasquarello, *Phys. Rev. B* **86**, 045112 (2012).
- ¹⁶ P. A. Schultz, *Phys. Rev. Lett.* **84**, 1942 (2000).
- ¹⁷ M. Leslie and N. J. Gillan, *J. Phys. C: Solid State Phys.* **18**, 973 (1985).
- ¹⁸ G. Makov and M. C. Payne, *Phys. Rev. B* **51**, 4014 (1995).
- ¹⁹ S. Lany and A. Zunger, *Phys. Rev. B* **78**, 235104 (2008).
- ²⁰ C. Freysoldt, J. Neugebauer, and C. G. V. de Walle, *Phys. Rev. Lett.* **102**, 016402 (2009).
- ²¹ T. L. Aselage, D. R. Tallant, and D. Emin, *Phys. Rev. B* **56**, 3122 (1997).
- ²² T. Stoto, N. Housseau, L. Zuppiroli, and B. Kryger, *J. Appl. Phys.* **68**, 3198 (1990).
- ²³ T. Stoto, L. Zuppiroli, and J. Pelissier, *Radiat. Eff.* **90**, 161 (1985).
- ²⁴ W. Tang, E. Sanville, and G. Henkelman, *J. Phys.: Condens. Matter* **21**, 084204 (2009).
- ²⁵ O. Cretu, Y.-C. Lin, and K. Suenaga, *Micron* **72**, 21 (2015).